

Large Photoelasticity in Topological Antiferromagnet Mn_3Sn Studied by Coherent Acoustic Phonon

Yuchen Wang^A, Takuya Matsuda^{A,B}, Yuta Murotani^A, Hanyi Peng^B, Takumi Matsuo^B,
Tomoya Higo^B, Satoru Nakatsuji^{A,B,C,D}, and Ryusuke Matsunaga^{A,C}

^A *The Institute for Solid State Physics, The University of Tokyo, Kashiwa, Chiba 277-8581, Japan*

^B *Department of Physics, The University of Tokyo, Bunkyo-ku, Tokyo, 113-0033, Japan*

^C *Trans-scale Quantum Science Institute, The University of Tokyo, Bunkyo-ku, Tokyo, 113-0033,
Japan*

^D *Institute for Quantum Matter and Department of Physics and Astronomy, Johns Hopkins
University, Baltimore, 21218 Maryland, USA*

Abstract:

We investigate the relation of electronic and optical properties to ultrafast strain in topological antiferromagnet Mn_3Sn thin films using near-infrared femtosecond laser pulses. Coherent acoustic phonon oscillations are generated and clearly identified with a remarkably large amplitude exceeding 1% in differential transmission. Quantitative analysis reveals that near-infrared photoelastic coefficient in Mn_3Sn is several times larger than that in typical materials. These results establish a quantitative approach for understanding the large optical responses to ultrafast strain in the topological kagome antiferromagnet, suggesting potential opto-spintronic and optoacoustic applications even at telecommunications wavelength.

Antiferromagnets (AFMs) have recently garnered great interest due to their potential for making spintronics with higher integration density and ultrafast processing speed, because of the absence of stray field and the fast precessional motion of AFM spins in terahertz (THz) regime¹⁻⁴. Particularly noteworthy is the non-collinear topological Weyl AFM Mn₃Sn⁵. Its crystalline structure is characterized by a stacked ABAB sequence of kagome bilayer, and the spins on Mn atoms within each kagome bilayer form an inverse triangular structure below $T_N \sim 430$ K⁶⁻⁹, which explicitly breaks the time-reversal symmetry (See Fig. 1(a)) despite negligibly small net magnetization. This unique spin structure gives rise to exceptionally large room-temperature responses across electrical, optical, and thermal channels, including a large anomalous Hall effect^{5,10}, a strong magneto-optical Kerr effect in the visible light range¹¹, a sizable Faraday effect in the THz regime¹², a pronounced anomalous Nernst effect¹³, and tunneling magnetoresistance in all-antiferromagnetic tunnel junctions¹⁴. The combination of ultrafast AFM spin dynamics and the pronounced electronic responsiveness to external stimuli at room temperature makes Mn₃Sn an exceptionally promising platform for AFM-based spintronics¹⁵. Consequently, a key next challenge is to achieve ultrafast manipulation of the AFM order. Recently, electric current-induced magnetic switching¹⁶⁻²⁰ and chiral spin rotation^{21,22} by the spin-orbit torque in Mn₃Sn/nonmagnetic metal bilayer structure have been reported as a promising pathway toward high-speed control of AFM spins. Furthermore, a large piezomagnetic effect, namely a linear coupling of magnetic order to strain, has also been reported in a bulk Mn₃Sn crystal so as to switch the AFM order by applying in-plane uniaxial strain on the order of 0.1%²³. A substrate-induced strain in the Mn₃Sn thin film also plays a crucial role in current-induced full switching between the AFM binary spin states¹⁸. These results exemplify the importance of strain and its considerable effect on magnetism²⁴⁻²⁶.

Recently, the speed of straintronics has been pushed up into the picosecond regime. Lattice distortions can be induced to control the spin states via nonlinear phonon excitation by intense laser pulses²⁷⁻²⁹ and the circular motion of ions in the lattice or substrate^{30,31}. Even in metals, where absorptions by infrared-active phonons are suppressed by electric screening, femtosecond optical pulses offer an alternative pathway to generate ultrafast strain in the form of coherent acoustic phonon (CAP), *i.e.* elastic wave³²⁻³⁴. CAP-induced modulation of magnetization in ferro- and ferrimagnets³⁵⁻³⁹ has been reported. Whether a similar strain-mediated high-speed control mechanism operates in Mn₃Sn remains an open question. Generally, ultrafast changes in magnetization can be probed by time-resolved magneto-optical Kerr effect (TR-MOKE) because the MOKE signal θ_K is proportional to the magnetization: $\theta_K = \alpha \times M$, where M is the magnetization and α is a proportional coefficient that depends on the complex refractive index. However, it should be noted that a TR-MOKE signal $\Delta\theta_K$ is not necessarily proportional to a change in magnetization ΔM because $\Delta\theta_K = \Delta\alpha \times M + \alpha \times \Delta M$. This relation indicates that, when the refractive index is significantly modulated by strain ($\Delta\alpha \neq 0$), a non-zero TR-MOKE signal ($\Delta\theta_K \neq 0$) can arise even if the magnetization

itself remains unchanged ($\Delta M = 0$). Indeed, a recent time-resolved terahertz Faraday rotation study on Mn_3Sn reported that the ultrafast change in Faraday rotation induced by femtosecond laser pulses is not explained by the change in the magnetic order⁴⁰. Therefore, for careful interpretation of the ultrafast strain-driven effects, it is critical to evaluate photoelasticity, *i.e.*, a strain-induced modulation of the optical refractive index. In addition, recent reports⁴¹ on kagome staircase oxides, such as $\text{Mg}_3\text{V}_2\text{O}_8$, have revealed large photostrictive responses. These effects arise from the pronounced structural anisotropy and buckled kagome geometry, which make the lattice exceptionally responsive to light-induced perturbations. Such observations suggest that kagome frameworks may support enhanced strain–optical coupling. This motivates exploring how strain modulates the ultrafast optical response in metallic kagome systems, including Mn_3Sn . The study of CAP and quantitative evaluation of photoelastic properties would provide valuable information for optoacoustic properties in this novel material.

In this work, we perform near-infrared (NIR) pump-probe spectroscopy to investigate the CAP dynamics and strain-induced optical response in Mn_3Sn thin films. We observe oscillations in the differential transmittance ($\Delta T/T$) with an amplitude as large as 1% in a 20 nm-thick film, and a frequency dependent on film thickness. The result is successfully reproduced by our analysis modeling the CAP generated by photoinduced heating in the films. Remarkably, the real part of the photoelastic coefficient in Mn_3Sn reaches approximately 24, several times larger than that of typical materials. Our quantitative analysis of the optical response in Mn_3Sn under ultrafast strain reveals its remarkable sensitivity to the strain, together with a robustness to intense photoirradiation, providing a strategy for picosecond strain-based control of AFM spins.

As depicted in Fig. 1(b), we used 15-40 nm-thick polycrystalline Mn_3Sn thin films grown on 500 μm -thick quartz (SiO_2) substrates⁴² (For details, see Supplementary Material S1). Optical pump pulse from Yb:KGW laser (PHAROS, Light Conversion) at a wavelength of 1030 nm with a duration of 160 fs and a repetition rate of 3 kHz were directed on the sample at a small angle to the normal incidence with a spot diameter of 0.45 mm. Subsequently, probe pulses of the same wavelength and duration with a smaller spot diameter 0.16 mm and weaker fluence of 50 $\mu\text{J cm}^{-2}$ were employed to detect the time-resolved pump-induced changes in transmittance by varying the delay time (Supplementary Material S2). All experiments were conducted at room temperature unless specifically stated.

Figure 2(a) shows representative results of transient differential transmission signals $\Delta T/T$ of a 20 nm-thick Mn_3Sn thin film. A pronounced oscillation in $\Delta T/T$ emerged at approximately 10 ps after photoexcitation. The non-oscillatory background was fitted using a bi-exponential function with a finite-rise onset (dashed line), and the residual oscillatory part was subsequently extracted. The oscillation $\Delta T_{\text{osc}}/T$ is well fitted by

$$\frac{\Delta T_{\text{osc}}}{T} = Ae^{-\frac{t}{\tau_d}} \cos(2\pi f_{\text{osc}}t + \varphi), \quad (1)$$

where A , τ_d , f_{osc} , and φ represent the amplitude, decay time, frequency, and initial phase of the oscillation, respectively. We varied the polarization direction of the probe pulse (not shown) and confirmed that no angular dependence was identified. The same approach was applied to samples of different thicknesses. In Fig. 2(b), we plot the oscillation amplitude as a function of the pump fluence. Remarkably, the amplitude exhibits a robust linear dependence on the pump fluence over the entire experimental range, up to the maximum value of approximately 3 mJ cm^{-2} . The oscillation amplitude reaches and even exceeds 1% in the thinner sample. The linear relationship and sharp oscillation amplitude are uncommon compared to typical materials, which will be discussed later.

Figure 2(c) presents the $\Delta T/T$ dynamics for films with various thicknesses. As the film thickness decreases, the oscillation becomes faster. By using Eq. (1), we obtained the corresponding oscillation frequency f_{osc} and damping rate $1/\tau_d$. The results are shown in Fig. 2(d). Both the oscillation frequency (left axis) and damping rate (right axis) are almost inversely proportional to the film thickness. To explain this, we consider a simple model for one-dimensional (1D) longitudinal standing wave inside the film. The corresponding frequency for each mode reads $f_{\text{sw}}^{(N)} = Nv/2d$, where N is a positive integer, v is the speed of sound in the sample, and d is the film thickness. Using the density $\rho=7440 \text{ kg/m}^3$, Young's modulus $E\sim 139 \text{ GPa}$, and Poisson's ratio $\nu=0.129$ for $\text{Mn}_3\text{Sn}^{43}$, we estimated $v = \sqrt{E(1-\nu)/\rho(1-\nu-2\nu^2)}=4.4 \text{ nm/ps}$. The solid curve in Fig. 2(d) shows the calculation of $f_{\text{sw}}^{(1)}$ for the fundamental ($N=1$) mode, which quantitatively agrees with the experiment. By considering the acoustic impedance mismatch between the sample and substrate, our calculation shows that the film vibrates like a quasi-two-free-end membrane, while partially transferring energy into the substrate. This corresponds to the CAP launched by impulsive photoexcitation with finite decay.

For more comprehensive analysis for the dynamical behavior of CAP, we developed the following model considering the thermoelasticity as a mechanism of CAP generation³³: A Gaussian-shaped 1030-nm pulse irradiates the Mn_3Sn film, serving as the heat source for the sample. Conversely, the silica substrate is transparent to this NIR light, resulting in no absorption and therefore no heat generation. Given that the spot sizes of both the pump and probe beams significantly exceed the sample thickness, a 1D model is sufficient to simulate the process. In the following, z denotes the perpendicular direction to the sample surface. We first established the heat equation,

$$\left(\frac{\partial}{\partial t} - \frac{k}{\rho c_p} \frac{\partial^2}{\partial z^2} \right) \Delta T_K(z, t) = s(z, t), \quad (2)$$

where $c_p=431 \text{ J/(kg}\cdot\text{K)}^{43}$, $\Delta T_K(z, t)$, and $s(z, t)$ are the heat capacity, temperature rise of

the lattice, and the laser-induced heat source, respectively. It is noteworthy that in the real scenario, the energy of the laser pulse directly couples to the electron system. Our calculation, based on the two-temperature model, indicates that the electron and lattice temperatures reach equilibrium within several ps as experimentally observed recently⁴⁰. Since we focus on longer timescale processes, we estimate the temperature rise by considering only the lattice temperature (see Supplementary Material S3 for details). Once the heat source is quantified, we can determine $\Delta T_K(z, t)$. Then we applied the elastic wave equation

$$\left(\frac{\partial^2}{\partial t^2} - v^2 \frac{\partial^2}{\partial z^2} - \frac{\eta}{\rho} \frac{\partial^3}{\partial z^2 \partial t} \right) u(z, t) = - \frac{\beta K}{\rho} \frac{\partial \Delta T_K(z, t)}{\partial z}, \quad (3)$$

where $\eta=10^{-3}$ Pa·s (see details in Supplementary Material S4), $\beta=3.8 \times 10^{-5}$ K⁻¹⁴⁴, $K=62 \times 10^9$ Pa⁴³, and $u(z, t)$ are the viscosity, linear expansion coefficient, bulk modulus, and the displacement due to the temperature rise, respectively. Thus, we obtained the values of the displacement $u(z, t)$ at a certain position z and other parameters such as the longitudinal strain $\eta_{33}(z, t) = \partial u(z, t) / \partial z$, stress $\sigma_{33}(z, t)$, etc. Additionally, we account for the boundary conditions that comprise continuity of heat flux and that of stress at the interfaces. The latter determines the damping of CAP, i.e., energy transfer into the substrate, due to acoustic impedance mismatch. The sample surface in contact with air is regarded as a free end, e.g., $\sigma_{33}(0, t)=0$.

Figure 3(a) presents the calculated results of the thickness change in the 25-nm sample, *i.e.*, $u(25, t) - u(0, t)$. We also determined the oscillation frequency and damping rate of CAP, which are plotted in Fig. 3(b) as open triangles and circles. The dynamical result in Fig. 3(a) shows a zigzag-shaped oscillation with a thermal background expansion, closely resembling the differential transmittance in Fig. 2(a). The waveform indicates a superposition of odd higher-order ($N = 3, 5, 7, \dots$) modes allowed by the boundary condition, a common feature in laser-induced CAP⁴⁵. In contrast to the fully zigzag oscillation in the simulation in Fig. 3(a), the experimentally observed second and third cycles of the oscillation in Fig. 2(a) evolve toward a sinusoid, suggesting the rapid damping of the higher-order modes. Nevertheless, the observed damping rate in Fig. 3(b) is in reasonable agreement with the calculation and scales with the oscillation frequency. The proportionality of $1/\tau_d \propto f_{osc}$ suggests that CAP energy is dissipated into the substrate for each expansion cycle. The result shows that, in spite of the fast relaxation of the higher-order modes to the fundamental mode, the acoustic energy remains mostly confined within the thin film and induces the remarkably large change in optical responses. Our calculations successfully reproduce both the oscillation frequency and the damping rate of $\Delta T_{osc}/T$, thereby demonstrating the generation of CAP by photoexcitation and allowing quantitative analysis for the acoustic response of Mn₃Sn thin films to sub-picosecond perturbations.

Figure 3(c) shows two-dimensional plots of the calculated temperature rise (upper) and strain (lower) as a function of the position z and the delay time t . Figure 3(d) shows spatial cross-sections of the strain at various delays, visualizing the time evolution of strain. The largest strain in the sample, corresponding to the peak as the arrow points in Fig. 3(a), reaches up to 0.3% at the highest fluence. Previous research showed that 0.1% static strain is sufficient to flip the spin orientation²³. The result highly suggests the possibility of manipulating the magnetization by strain induced by the optical pump. In the present experiment, however, the sample temperature is expected to be elevated from 300 to 468 K, exceeding T_N . Lowering the base temperature⁴⁶ or attaching a thermoelastic transducer³⁵⁻³⁹ may provide promising pathways toward realizing ultrafast, strain-induced control of AFM spins, which will be explored in future studies.

In this work, we focus on the remarkably large differential transmittance signal, reaching up to 1% in Fig. 2(a). From the analysis shown in Fig. 3(a), the relative thickness change at the oscillation maximum is estimated to be on the order of $\Delta d/d \sim 10^{-3}$. This is a common value compared with previous studies of CAP, which is reasonable given the elastic parameters of Mn_3Sn used in Eq. (3) are not exceptional⁴³. These results indicate that the origin of the exceptionally large oscillation amplitude observed in Fig. 2 does not originate from the magnitude of thickness modulation but should rather be from an enhanced strain-induced optical response. This property is quantified by a NIR photoelasticity, described by a complex photoelastic coefficient $\partial \tilde{n}_1 / \partial \eta_{33}$, which gives a change in complex refractive index $\tilde{n}_1 = n_1 + i\kappa_1$ per unit strain. Considering the theory of the photoelasticity^{32,47,48}, the strain-induced transient differential transmission could be written as

$$\frac{\Delta T}{T} = 2\text{Re} \left\{ ik_0 \frac{\partial \tilde{n}_1}{\partial \eta_{33}} \left[\frac{r_1}{1 + r_0 r_1 e^{2i\delta_0}} \int_0^d \eta_{33}(z, t) e^{2ik_1(d-z)} dz - \frac{r_0}{1 + r_0 r_1 e^{2i\delta_0}} \int_0^d \eta_{33}(z, t) e^{2ik_1 z} dz + \left(\frac{1 - r_0 r_1 e^{2i\delta_0}}{1 + r_0 r_1 e^{2i\delta_0}} \right) \int_0^d \eta_{33}(z, t) dz \right] \right\}. \quad (4)$$

where k_0 represents the probe wave vector in vacuum, r_0 and r_1 are the amplitude reflectance coefficients of air/ Mn_3Sn interface and $\text{Mn}_3\text{Sn}/\text{SiO}_2$ interface, respectively, and $\delta_0 = k_0 \tilde{n}_1 d$ is the undisturbed complex optical phase. Note that the integral of strain, in the third term on the right-hand side, represents the thickness change, which macroscopically reflects the strain distribution. To solve Eq. (4) using experimentally obtained $\Delta T_{\text{osc}}/T$, there are two unknown parameters: real- and imaginary-part photoelastic coefficient $\partial n_1 / \partial \eta_{33}$ and $\partial \kappa_1 / \partial \eta_{33}$. Using data from films with different thicknesses, we performed a global fit by assuming a common, thickness-independent photoelastic coefficient (find details in Supplementary Material S6). We calculated the strain distribution in Eq. (4) for each thickness and set the photoelastic coefficient as the only variable complex global parameter. Figure 4(a) shows the global fitting curves of 20, 25, 30, and 40 nm samples, where the fitted curves agree well with the experimental results. We obtained the average value from 1000 fitting runs and compared the result for

Mn₃Sn with those reported previously for other materials^{48–50}, as plotted in Fig. 4(b). The photoelastic coefficient in Mn₃Sn was evaluated as $\partial\tilde{n}_1/\partial\eta_{33} \sim 23.9(\pm 1.2) - i8.4(\pm 1.4)$, which is several times larger than that of the traditional metals that we used for comparison.

To check the relation between the exceptionally large photoelastic response in Mn₃Sn and its AFM order, we investigated the temperature dependence of CAP. Figure 4(c) plots the oscillation amplitude as a function of the base temperature for the 15-nm sample. At around 250 K, where a spin reorientation phase transition to a helical phase occurs⁵¹, the data exhibits a slight jump. A recent study showed that a lattice expansion is accompanied with the helical phase transition⁴³, suggesting a change in mechanical parameters. Notably, even at a high temperature close to T_N , the oscillation amplitude remains large, suggesting that the large photoelasticity is not directly tied to the inverse-triangular AFM phase. This result implies that the large photoelastic response may be a more universal feature of kagome materials, in which the lattice symmetry is directly connected to electronics properties⁵². We propose several possible contributing factors: (1) Flat band. The kagome materials are known to host flat bands^{53,54}, where band dispersion is nearly zero and electron effective mass becomes large. The resulting large density of states (DOS) enhances the electronic correlation effects⁵⁵ and may also contribute to a stronger electron-phonon coupling. (2) Van Hove singularity. ARPES measurements⁵⁶ show that the van Hove singularity appears at the M point in momentum space. This saddle-point structure also leads to a high DOS, making electrons more susceptible to external perturbations such as lattice distortions. In addition, the energy separation between van Hove singularity and E_F is approximately 100 meV, which is relatively small and may further amplify the electronic response.

In summary, we observed large oscillations of differential transmittance exceeding 1% in photoexcited Mn₃Sn thin films, exhibiting a robust linear dependence on pump fluence. Quantitative analysis based on heat-driven CAP reproduces the experimental results and reveals the remarkably large photoelastic coefficient of Mn₃Sn in the near-infrared region, compared with typical materials. The large strain-induced optical response provides a sensitive probe for tracking the ultrafast post-pump dynamics. More importantly, strain emerges as an efficient pathway for investigating topological Weyl magnets. Our work establishes a quantitative route to generate and control ultrafast strain in Mn₃Sn films on demand and further pave the way for investigations of coupled electron-phonon-magnon dynamics. Furthermore, the near-infrared response of Mn₃Sn suggests that similar mechanisms could be exploited toward telecommunications-band operation, offering potential compatibility with photonic-circuit architectures designed for this spectral region.

References

- ¹ V. Baltz, A. Manchon, M. Tsoi, T. Moriyama, T. Ono, and Y. Tserkovnyak, “Antiferromagnetic spintronics,” *Rev. Mod. Phys.* **90**(1), 015005 (2018).
- ² P. Němec, M. Fiebig, T. Kampfrath, and A.V. Kimel, “Antiferromagnetic opto-spintronics,” *Nat. Phys.* **14**(3), 229–241 (2018).
- ³ L. Šmejkal, A.H. MacDonald, J. Sinova, S. Nakatsuji, and T. Jungwirth, “Anomalous Hall antiferromagnets,” *Nat. Rev. Mater.* **7**(6), 482–496 (2022).
- ⁴ J. Han, R. Cheng, L. Liu, H. Ohno, and S. Fukami, “Coherent antiferromagnetic spintronics,” *Nat. Mater.* **22**(6), 684–695 (2023).
- ⁵ S. Nakatsuji, N. Kiyohara, and T. Higo, “Large anomalous Hall effect in a non-collinear antiferromagnet at room temperature,” *Nature* **527**(7577), 212–215 (2015).
- ⁶ E. Krén, J. Paitz, G. Zimmer, and É. Zsoldos, “Study of the magnetic phase transformation in the Mn_3Sn phase,” *Physica B+C* **80**(1), 226–230 (1975).
- ⁷ S. Tomiyoshi, and Y. Yamaguchi, “Magnetic Structure and Weak Ferromagnetism of Mn_3Sn Studied by Polarized Neutron Diffraction,” *J. Phys. Soc. Jpn.* **51**(8), 2478–2486 (1982).
- ⁸ T. Nagamiya, S. Tomiyoshi, and Y. Yamaguchi, “Triangular spin configuration and weak ferromagnetism of Mn_3Sn and Mn_3Ge ,” *Solid State Commun.* **42**(5), 385–388 (1982).
- ⁹ P.J. Brown, V. Nunez, F. Tasset, J.B. Forsyth, and P. Radhakrishna, “Determination of the magnetic structure of Mn_3Sn using generalized neutron polarization analysis,” *J. Phys.: Condens. Matter* **2**(47), 9409–9422 (1990).
- ¹⁰ J. Kübler, and C. Felser, “Non-collinear antiferromagnets and the anomalous Hall effect,” *EPL* **108**(6), 67001 (2014).
- ¹¹ T. Higo, H. Man, D.B. Gopman, L. Wu, T. Koretsune, O.M.J. van ’t Erve, Y.P. Kabanov, D. Rees, Y. Li, M.-T. Suzuki, S. Patankar, M. Ikhlas, C.L. Chien, R. Arita, R.D. Shull, J. Orenstein, and S. Nakatsuji, “Large magneto-optical Kerr effect and imaging of magnetic octupole domains in an antiferromagnetic metal,” *Nat. Photonics* **12**(2), 73–78 (2018).
- ¹² T. Matsuda, N. Kanda, T. Higo, N.P. Armitage, S. Nakatsuji, and R. Matsunaga, “Room-temperature terahertz anomalous Hall effect in Weyl antiferromagnet Mn_3Sn thin films,” *Nat. Commun.* **11**(1), 909 (2020).
- ¹³ M. Ikhlas, T. Tomita, T. Koretsune, M.-T. Suzuki, D. Nishio-Hamane, R. Arita, Y. Otani, and S. Nakatsuji, “Large anomalous Nernst effect at room temperature in a chiral antiferromagnet,” *Nat. Phys.* **13**(11), 1085–1090 (2017).
- ¹⁴ X. Chen, T. Higo, K. Tanaka, T. Nomoto, H. Tsai, H. Idzuchi, M. Shiga, S. Sakamoto, R. Ando, H. Kosaki, T. Matsuo, D. Nishio-Hamane, R. Arita, S. Miwa, and S. Nakatsuji, “Octupole-driven magnetoresistance in an antiferromagnetic tunnel junction,” *Nature* **613**(7944), 490–495 (2023).
- ¹⁵ S. Nakatsuji, and R. Arita, “Topological Magnets: Functions Based on Berry Phase and Multipoles,” *Annu. Rev. Condens. Matter Phys.* **13**(1), 119–142 (2022).
- ¹⁶ H. Tsai, T. Higo, K. Kondou, T. Nomoto, A. Sakai, A. Kobayashi, T. Nakano, K. Yakushiji, R. Arita, S. Miwa, Y. Otani, and S. Nakatsuji, “Electrical manipulation of a topological antiferromagnetic state,” *Nature* **580**(7805), 608–613 (2020).

- ¹⁷ Y. Deng, R. Li, and X. Liu, “Thickness dependent anomalous Hall effect in noncollinear antiferromagnetic Mn₃Sn polycrystalline thin films,” *J. Alloys Compd.* **874**, 159910 (2021).
- ¹⁸ T. Higo, K. Kondou, T. Nomoto, M. Shiga, S. Sakamoto, X. Chen, D. Nishio-Hamane, R. Arita, Y. Otani, S. Miwa, and S. Nakatsuji, “Perpendicular full switching of chiral antiferromagnetic order by current,” *Nature* **607**(7919), 474–479 (2022).
- ¹⁹ G.K. Krishnaswamy, G. Sala, B. Jacot, C.-H. Lambert, R. Schlitz, M.D. Rossell, P. Noël, and P. Gambardella, “Time-Dependent Multistate Switching of Topological Antiferromagnetic Order in Mn₃Sn,” *Phys. Rev. Appl.* **18**(2), 024064 (2022).
- ²⁰ K. Ogawa, H. Tsai, N. Yoshikawa, T. Matsuo, Y. Tsushima, M. Asakura, H. Peng, T. Matsuda, T. Higo, S. Nakatsuji, and R. Shimano, “Ultrafast time-resolved observation of non-thermal current-induced switching in an antiferromagnetic Weyl semimetal,” *Nat. Mater.*, (2025).
- ²¹ Y. Takeuchi, Y. Yamane, J.-Y. Yoon, R. Itoh, B. Jinnai, S. Kanai, J. Ieda, S. Fukami, and H. Ohno, “Chiral-spin rotation of non-collinear antiferromagnet by spin-orbit torque,” *Nat. Mater.* **20**(10), 1364–1370 (2021).
- ²² Y. Takeuchi, Y. Sato, Y. Yamane, J.-Y. Yoon, Y. Kanno, T. Uchimura, K.V. De Zoysa, J. Han, S. Kanai, J. Ieda, H. Ohno, and S. Fukami, “Electrical coherent driving of chiral antiferromagnet,” *Science* **389**(6762), 830–834 (2025).
- ²³ M. Ikhlas, S. Dasgupta, F. Theuss, T. Higo, S. Kittaka, B.J. Ramshaw, O. Tchernyshyov, C.W. Hicks, and S. Nakatsuji, “Piezomagnetic switching of the anomalous Hall effect in an antiferromagnet at room temperature,” *Nat. Phys.* **18**(9), 1086–1093 (2022).
- ²⁴ R. Ramesh, and N.A. Spaldin, “Multiferroics: progress and prospects in thin films,” *Nat. Mater.* **6**(1), 21–29 (2007).
- ²⁵ Z.Q. Liu, H. Chen, J.M. Wang, J.H. Liu, K. Wang, Z.X. Feng, H. Yan, X.R. Wang, C.B. Jiang, J.M.D. Coey, and A.H. MacDonald, “Electrical switching of the topological anomalous Hall effect in a non-collinear antiferromagnet above room temperature,” *Nat. Electron.* **1**(3), 172–177 (2018).
- ²⁶ H. Yan, Z. Feng, S. Shang, X. Wang, Z. Hu, J. Wang, Z. Zhu, H. Wang, Z. Chen, H. Hua, W. Lu, J. Wang, P. Qin, H. Guo, X. Zhou, Z. Leng, Z. Liu, C. Jiang, M. Coey, and Z. Liu, “A piezoelectric, strain-controlled antiferromagnetic memory insensitive to magnetic fields,” *Nat. Nanotechnol.* **14**(2), 131–136 (2019).
- ²⁷ S.F. Maehrlein, I. Radu, P. Maldonado, A. Paarmann, M. Gensch, A.M. Kalashnikova, R.V. Pisarev, M. Wolf, P.M. Oppeneer, J. Barker, and T. Kampfrath, “Dissecting spin-phonon equilibration in ferrimagnetic insulators by ultrafast lattice excitation,” *Sci. Adv.* **4**(7), eaar5164 (2018).
- ²⁸ D. Afanasiev, J.R. Hortensius, B.A. Ivanov, A. Sasani, E. Bousquet, Y.M. Blanter, R.V. Mikhaylovskiy, A.V. Kimel, and A.D. Caviglia, “Ultrafast control of magnetic interactions via light-driven phonons,” *Nat. Mater.* **20**(5), 607–611 (2021).
- ²⁹ A. Stupakiewicz, C.S. Davies, K. Szerenos, D. Afanasiev, K.S. Rabinovich, A.V. Boris, A. Caviglia, A.V. Kimel, and A. Kirilyuk, “Ultrafast phononic switching of magnetization,” *Nat. Phys.* **17**(4), 489–492 (2021).

- ³⁰ T.F. Nova, A. Cartella, A. Cantaluppi, M. Först, D. Bossini, R.V. Mikhaylovskiy, A.V. Kimel, R. Merlin, and A. Cavalleri, “An effective magnetic field from optically driven phonons,” *Nat. Phys.* **13**(2), 132–136 (2017).
- ³¹ C.S. Davies, F.G.N. Fennema, A. Tsukamoto, I. Razdolski, A.V. Kimel, and A. Kirilyuk, “Phononic switching of magnetization by the ultrafast Barnett effect,” *Nature* **628**, 540–544 (2024).
- ³² O. Matsuda, M.C. Larciprete, R. Li Voti, and O.B. Wright, “Fundamentals of picosecond laser ultrasonics,” *Ultrasonics* **56**, 3–20 (2015).
- ³³ P. Ruello, and V.E. Gusev, “Physical mechanisms of coherent acoustic phonons generation by ultrafast laser action,” *Ultrasonics* **56**, 21–35 (2015).
- ³⁴ F. Vialla, and N.D. Fatti, “Time-Domain Investigations of Coherent Phonons in van der Waals Thin Films,” *Nanomaterials* **10**(12), 2543 (2020).
- ³⁵ C. Pfaff, T. Pezeril, R. Arras, L. Calmels, V. Cherruault, S. Andrieu, K. Dumesnil, J. Gorchon, and T. Hauet, “Strain-induced magnetic moment variations at the picosecond timescale,” *Phys. Rev. B* **111**(6), 064405 (2025).
- ³⁶ M. Deb, E. Popova, M. Hehn, N. Keller, S. Mangin, and G. Malinowski, “Picosecond acoustic-excitation-driven ultrafast magnetization dynamics in dielectric Bi-substituted yttrium iron garnet,” *Phys. Rev. B* **98**(17), 174407 (2018).
- ³⁷ J.V. Jäger, A.V. Scherbakov, T.L. Linnik, D.R. Yakovlev, M. Wang, P. Wadley, V. Holy, S.A. Cavill, A.V. Akimov, A.W. Rushforth, and M. Bayer, “Picosecond inverse magnetostriction in galfenol thin films,” *Appl. Phys. Lett.* **103**(3), 032409 (2013).
- ³⁸ J.-W. Kim, M. Vomir, and J.-Y. Bigot, “Ultrafast Magnetoacoustics in Nickel Films,” *Phys. Rev. Lett.* **109**(16), 166601 (2012).
- ³⁹ A.V. Scherbakov, A.S. Salasyuk, A.V. Akimov, X. Liu, M. Bombeck, C. Brüggemann, D.R. Yakovlev, V.F. Sapega, J.K. Furdyna, and M. Bayer, “Coherent Magnetization Precession in Ferromagnetic (Ga,Mn)As Induced by Picosecond Acoustic Pulses,” *Phys. Rev. Lett.* **105**(11), 117204 (2010).
- ⁴⁰ T. Matsuda, T. Higo, T. Koretsune, N. Kanda, Y. Hirai, H. Peng, T. Matsuo, N. Yoshikawa, R. Shimano, S. Nakatsuji, and R. Matsunaga, “Ultrafast Dynamics of Intrinsic Anomalous Hall Effect in the Topological Antiferromagnet Mn_3Sn ,” *Phys. Rev. Lett.* **130**(12), 126302 (2023).
- ⁴¹ M.A. Boda, C. Chen, X. He, and Z. Yi, “Photostriction in emerging inorganic materials for next-generation micro-optomechanical devices,” *Appl. Phys. Rev.* **12**(3), 031307 (2025).
- ⁴² T. Higo, D. Qu, Y. Li, C.L. Chien, Y. Otani, and S. Nakatsuji, “Anomalous Hall effect in thin films of the Weyl antiferromagnet Mn_3Sn ,” *Appl. Phys. Lett.* **113**(20), 202402 (2018).
- ⁴³ M. Ikhlas, K.R. Shirer, P.-Y. Yang, A.P. Mackenzie, S. Nakatsuji, and C.W. Hicks, “A tunable stress dilatometer and measurement of the thermal expansion under uniaxial stress of Mn_3Sn ,” *Appl. Phys. Lett.* **117**(23), 233502 (2020).
- ⁴⁴ Y. Song, Y. Qiao, Q. Huang, C. Wang, X. Liu, Q. Li, J. Chen, and X. Xing, “Opposite Thermal Expansion in Isostructural Noncollinear Antiferromagnetic Compounds of

Mn₃A (A = Ge and Sn),” *Chem. Mater.* **30**(18), 6236–6241 (2018).

⁴⁵ F. Hudert, A. Bruchhausen, D. Issenmann, O. Schecker, R. Waitz, A. Erbe, E. Scheer, T. Dekorsy, A. Mlayah, and J.-R. Huntzinger, “Confined longitudinal acoustic phonon modes in free-standing Si membranes coherently excited by femtosecond laser pulses,” *Phys. Rev. B* **79**(20), 201307 (2009).

⁴⁶ D.J. Lovinger, E. Zoghlin, P. Kissin, G. Ahn, K. Ahadi, P. Kim, M. Poore, S. Stemmer, S.J. Moon, S.D. Wilson, and R.D. Averitt, “Magnetoelastic coupling to coherent acoustic phonon modes in the ferrimagnetic insulator GdTO₃,” *Phys. Rev. B* **102**(8), 085138 (2020).

⁴⁷ C. Thomsen, H.T. Grahn, H.J. Maris, and J. Tauc, “Surface generation and detection of phonons by picosecond light pulses,” *Phys. Rev. B* **34**(6), 4129–4138 (1986).

⁴⁸ S. Wu, Z. Lu, A. Hu, X. Miao, F. Wang, Z. Sun, H. Yan, H. Zhang, and M. Ji, “Dichroic Photoelasticity in Black Phosphorus Revealed by Ultrafast Coherent Phonon Dynamics,” *J. Phys. Chem. Lett.* **12**(25), 5871–5878 (2021).

⁴⁹ T. Saito, O. Matsuda, and O.B. Wright, “Picosecond acoustic phonon pulse generation in nickel and chromium,” *Phys. Rev. B* **67**(20), 205421 (2003).

⁵⁰ O. Matsuda, T. Tachizaki, T. Fukui, J.J. Baumberg, and O.B. Wright, “Acoustic phonon generation and detection in GaAs/Al_{0.3}Ga_{0.7}As quantum wells with picosecond laser pulses,” *Phys. Rev. B* **71**(11), 115330 (2005).

⁵¹ T.F. Duan, W.J. Ren, W.L. Liu, S.J. Li, W. Liu, and Z.D. Zhang, “Magnetic anisotropy of single-crystalline Mn₃Sn in triangular and helix-phase states,” *Appl. Phys. Lett.* **107**(8), 082403 (2015).

⁵² J.-X. Yin, B. Lian, and M.Z. Hasan, “Topological kagome magnets and superconductors,” *Nature* **612**(7941), 647–657 (2022).

⁵³ J.-X. Yin, N. Shumiya, S. Mardanya, Q. Wang, S.S. Zhang, H.-J. Tien, D. Multer, Y. Jiang, G. Cheng, N. Yao, S. Wu, D. Wu, L. Deng, Z. Ye, R. He, G. Chang, Z. Liu, K. Jiang, Z. Wang, T. Neupert, A. Agarwal, T.-R. Chang, C.-W. Chu, H. Lei, and M.Z. Hasan, “Fermion–boson many-body interplay in a frustrated kagome paramagnet,” *Nat. Commun.* **11**(1), 4003 (2020).

⁵⁴ S.S. Zhang, J.-X. Yin, M. Ikhlas, H.-J. Tien, R. Wang, N. Shumiya, G. Chang, S.S. Tsirkin, Y. Shi, C. Yi, Z. Guguchia, H. Li, W. Wang, T.-R. Chang, Z. Wang, Y. Yang, T. Neupert, S. Nakatsuji, and M.Z. Hasan, “Many-Body Resonance in a Correlated Topological Kagome Antiferromagnet,” *Phys. Rev. Lett.* **125**(4), 046401 (2020).

⁵⁵ T. Matsuda, T. Higo, K. Kuroda, T. Koretsune, N. Kanda, Y. Hirai, H. Peng, T. Matsuo, C. Bareille, A. Varykhalov, N. Yoshikawa, J. Yoshinobu, T. Kondo, R. Shimano, S. Nakatsuji, and R. Matsunaga, “Emergence of high-mobility carriers in topological kagome bad metal Mn₃Sn by intense photoexcitation,” *Phys. Rev. Mater.* **9**(1), 014202 (2025).

⁵⁶ K. Kuroda, T. Tomita, M.-T. Suzuki, C. Bareille, A.A. Nugroho, P. Goswami, M. Ochi, M. Ikhlas, M. Nakayama, S. Akebi, R. Noguchi, R. Ishii, N. Inami, K. Ono, H. Kumigashira, A. Varykhalov, T. Muro, T. Koretsune, R. Arita, S. Shin, T. Kondo, and S. Nakatsuji, “Evidence for magnetic Weyl fermions in a correlated metal,” *Nat. Mater.*

16(11), 1090–1095 (2017).

SUPPLEMENTARY MATERIALS

Supporting Information is available from the Wiley Online Library or from the author, which includes the supplementary material for sample preparation, experimental setup, theoretical model and calculation of the CAP, derivation of the relationship between $\Delta T/T$ and CAP, and more details.

AUTHOR DECLARATIONS

Conflict of Interest

The authors have no conflicts to disclose.

Author Contributions

This work was supported by JST Mirai Program (Grant No. JPMJMI20A1), JSPS KAKENHI (Grant No. JP24K16990), and JST SPRING (Grant No. JPMJSP2108). T.M. and R.M. conceived this project. H.P., T.M., T.H., and S.N. fabricated the samples. Y.W. and T.M. constructed the optical setup and performed the experiments. Y.M. and Y.W. conducted theoretical analysis. Y.W. and R.M. wrote the manuscript with substantial feedback from T.M., Y.M., T.H., and all the coauthors.

DATA AVAILABILITY

The data that support the findings of this study are available from the corresponding author upon reasonable request.

Figures and legends

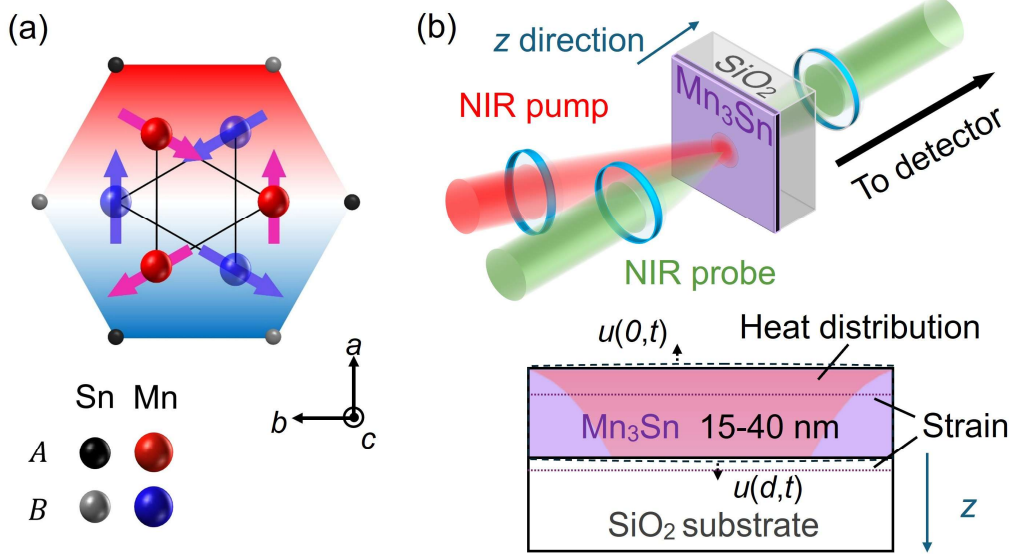


Fig. 1. (a) Crystal and magnetic structure of the non-collinear antiferromagnet Mn_3Sn . The magenta and blue arrows represent the spin of Mn atoms in A and B layer, respectively. (b) Schematic diagrams of the sample/substrate structure and the near-infrared (NIR) pump-probe spectroscopy configuration. For clarity, pump and probe beams are illustrated in different colors. Upper: Three-dimensional illustration of experimental geometry. Lower: Two-dimensional cross-sectional view of the photoexcited film structure. The strain field is generated in both the Mn_3Sn and SiO_2 substrate. For simplicity, a δ -function strain profile is shown.

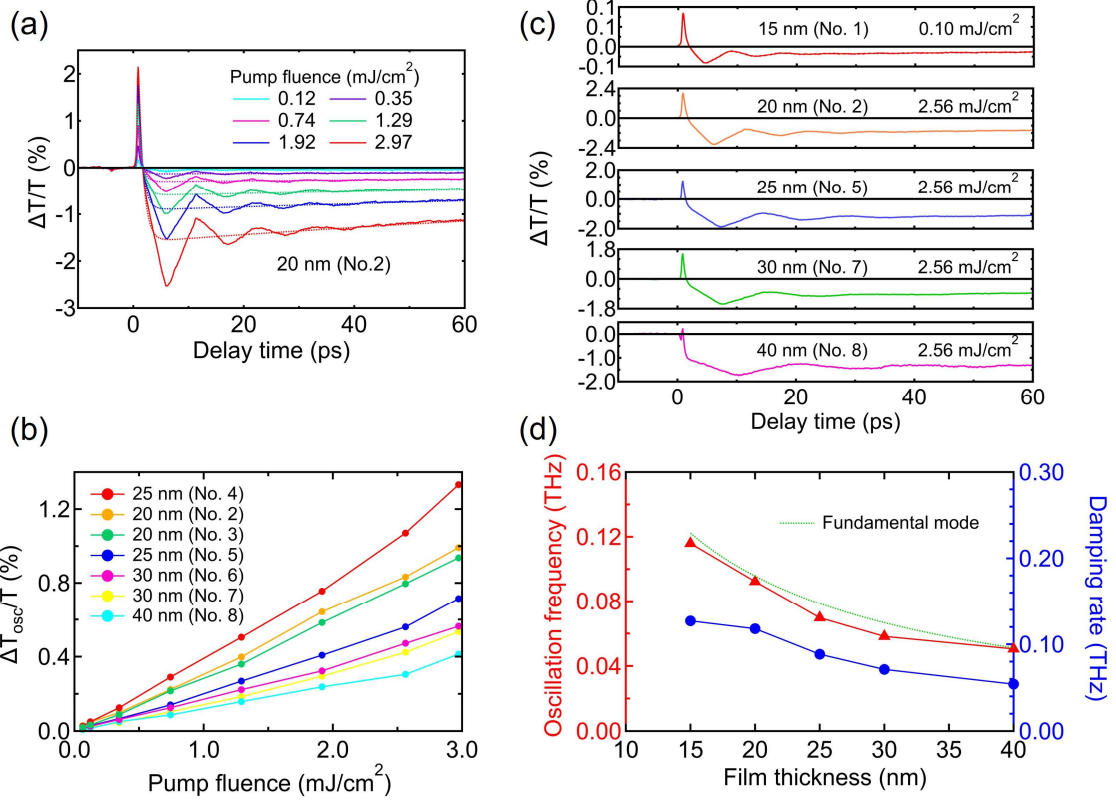


Fig. 2. (a) $\Delta T/T$ in 20 nm-thick Mn₃Sn thin film at different pump fluences. (b) Dependence of peak-to-zero oscillation amplitude on pump fluence. (c) $\Delta T/T$ in 15-40 nm films. (d) Dependence of oscillation frequency and damping rate on film thickness. The green dashed line shows the fundamental frequency of the standing wave, which agrees well with the experimental results.

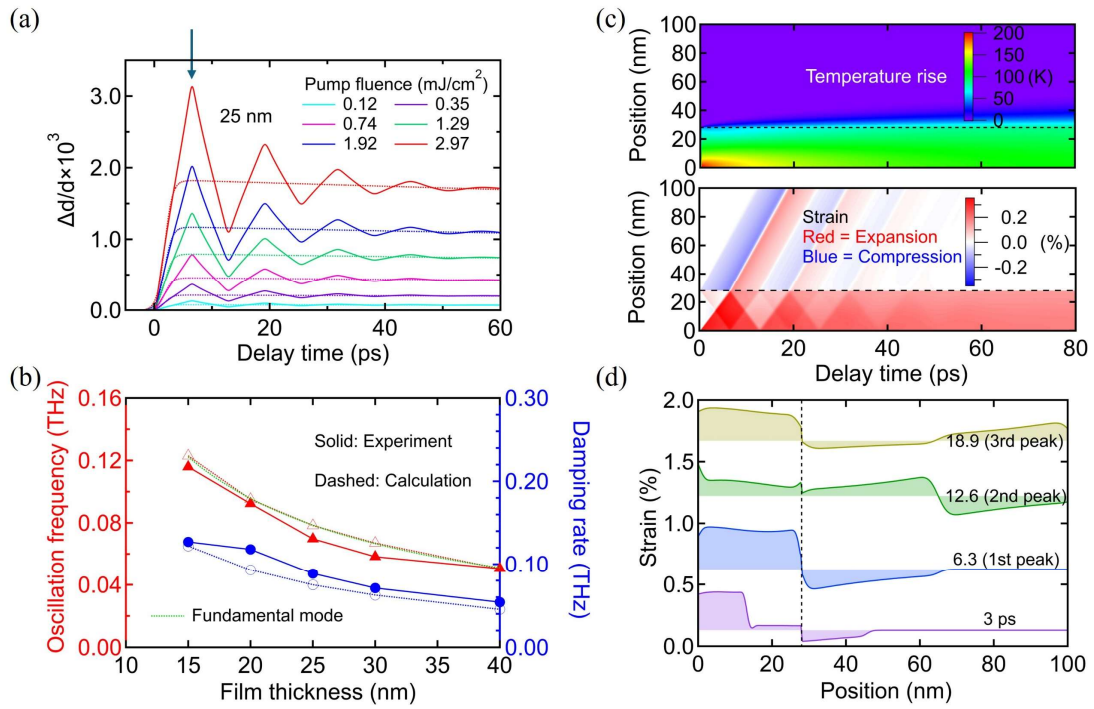


Fig. 3. (a) Calculation of the thickness change in 25 nm sample. The arrow points at the first peak. (b) Comparison of the oscillation frequency and damping rate. The solid lines with filled markers and dashed lines with open markers show results of the experimental observations of $\Delta T_{osc}/T$, and theoretical calculations of $\Delta d_{osc}/d$, respectively. (c) Time-dependent evolution of the temperature (upper) and strain (lower) in the 25 nm sample and substrate. The dashed black lines represent the interface. (d) Spatial cross-sections of the strain evolution at various delays.

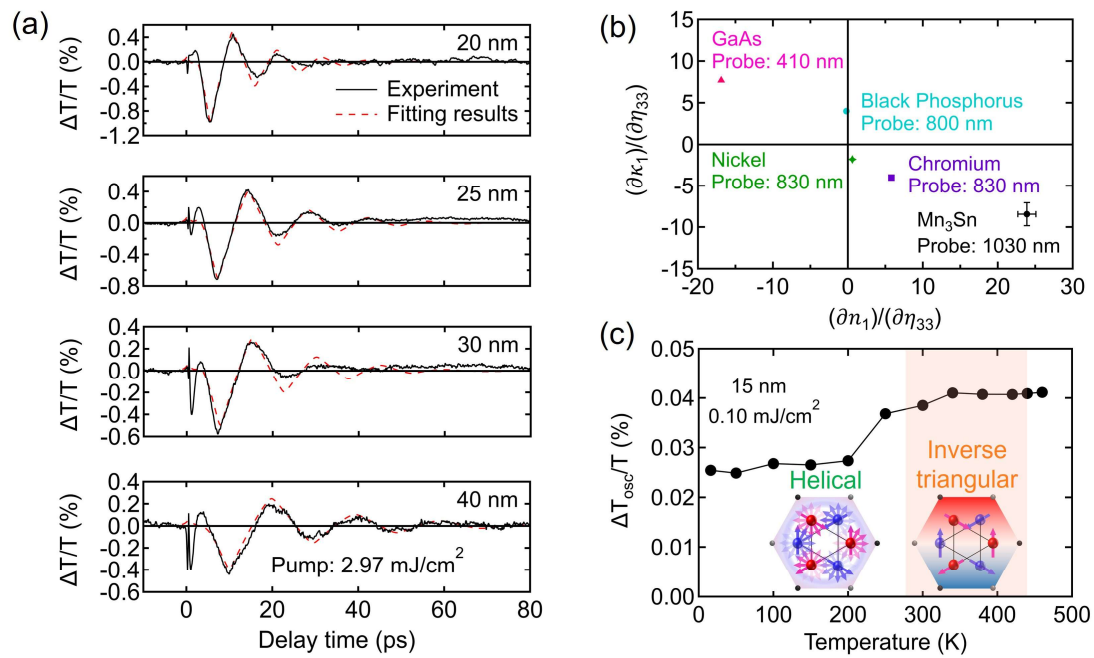


Fig. 4. (a) Global fitting results of 20 nm (No. 2), 25 nm (No. 5), 30 nm (No. 7), and 40 nm (No. 8). The black solid lines are the experimental results, and red dashed lines correspond to global fitting results obtained by Eq. (4). (b) Complex photoelastic coefficient of Mn_3Sn thin films and comparison with other materials. (c) Temperature dependence of oscillation amplitude in 15 nm film. A clear decrease at ~ 250 K is observed. Inset panels show the top views of the magnetic order at each phase.

Supplementary materials

S1. Sample fabrication

Mn₃Sn polycrystalline thin films (15-40 nm) were deposited on 500 μm-thick quartz (SiO₂) substrates by DC magnetron sputtering from a Mn_{2.7}Sn alloy target in a chamber with a base pressure of $< 5 \times 10^{-7}$ Pa. An AlO_x passivation layer (3 nm) was subsequently deposited by RF magnetron sputtering. Both the Mn₃Sn and AlO_x layers were prepared at room temperature, followed by annealing at 500 °C for 30 minutes. The sputtering power was 60 W for Mn₃Sn, and 100 W for AlO_x. The composition of the Mn₃Sn layers was determined as Mn_{3.1}Sn_{0.9} for sample No. 1 (15 nm), No. 2 (20 nm), No. 5 (25 nm), No. 7 (30 nm) and Mn_{2.98}Sn_{1.02} for sample No. 3 (20 nm), No. 4 (25 nm), No. 6 (30 nm), No. 8 (40 nm) by scanning electron microscopy-energy dispersive X-ray spectrometry (SEM-EDX).

S2. Experimental setup

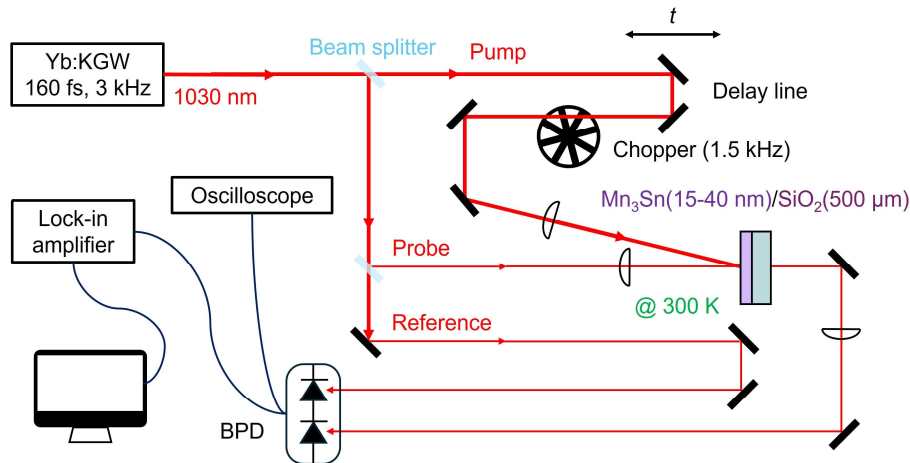


Fig. S1. Experimental setup for pump-probe differential spectroscopy. BPD: a balanced photodiode.

S3. Two-temperature model

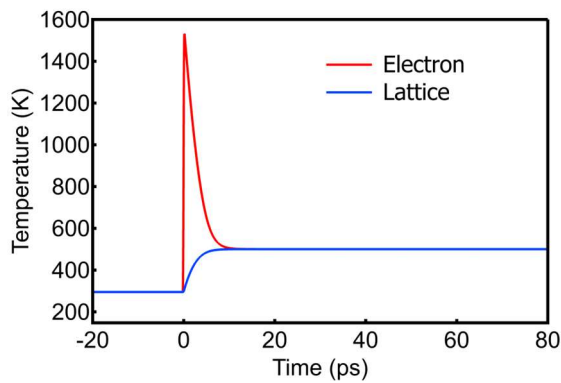


Fig. S2. Calculation of electron and lattice temperature.

Figure S2 shows the calculation of electron temperature T_e and lattice temperature T_l based on the two-temperature model:

$$C_e \frac{\partial T_e}{\partial t} = s(t) - g(T_e - T_l), \quad (\text{S1})$$

$$C_l \frac{\partial T_l}{\partial t} = g(T_e - T_l), \quad (\text{S2})$$

where $C_e = 596 \text{ J m}^{-3} \text{ K}^{-1}$, $C_l = 3.3 \times 10^6 \text{ J m}^{-3} \text{ K}^{-1}$, and $g = 1.8 \times 10^5 \text{ J ps}^{-1} \text{ m}^{-3} \text{ K}^{-1}$ [S1, S2] represents the electron heat capacity, lattice heat capacity, and electron-phonon coupling coefficient, respectively. Here the initial temperature is set to be 295 K and the pump fluence is 3 mJ cm^{-2} . We obtained that the electron and lattice temperatures reach equilibrium at $\sim 10 \text{ ps}$. Since we focus on oscillatory behavior, we only consider the lattice temperature in the CAP calculation. The sub-picosecond peak observed in the $\Delta T/T$ is attributed to the ultrafast electronic response as shown by the red curve in Fig. S2.

S4. Evaluation of viscosity and its influence on CAP

In the main text, we evaluate the viscosity of Mn_3Sn films to be $\eta = 10^{-3} \text{ Pa}\cdot\text{s}$. We refer to the values of some similar metallic materials in ref. [S3] and values of iron and copper in ref. [S4], and evaluate viscosity $\eta \sim 3 \times 10^{-4} \text{ Pa}\cdot\text{s}$. In conservative calculation, we used $10^{-3} \text{ Pa}\cdot\text{s}$ (larger viscous damping) to avoid overestimating the oscillation amplitude of $\Delta d/d$. As shown in Fig. S3, the result does not change much by changing the viscosity from 10^{-4} to $10^{-3} \text{ Pa}\cdot\text{s}$.

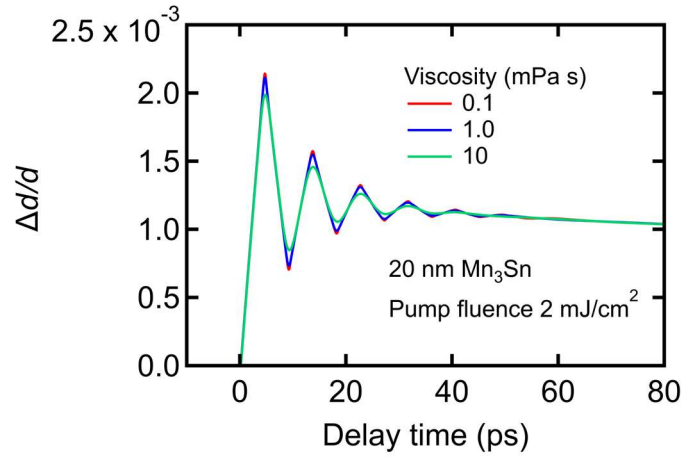


Fig. S3. $\Delta d/d$ in 20-nm sample for a pump fluence of 2 mJ cm^{-2} , considering different viscosity.

S5. Equation for optical detection

The theoretical model is shown by Fig. S4.

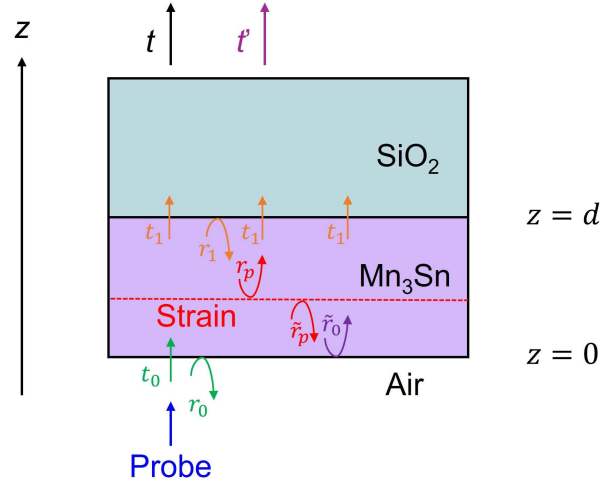


Fig. S4. Influence of strain to probe light transmittance in two-layer system.

Considering multi-reflection without perturbation, the original amplitude transmission coefficient is:

$$t = t_0 e^{i\delta_0} t_1 + t_0 r_1 \tilde{r}_0 e^{i3\delta_0} t_1 + t_0 r_1 \tilde{r}_0 r_1 \tilde{r}_0 e^{i5\delta_0} t_1 + \dots \quad (\text{S3})$$

It is a geometric sequence with common ratio $q = -r_1 \tilde{r}_0 e^{i2\delta_0}$, thus we obtain

$$t = t_0 t_1 e^{i\delta_0} M_{MR} = \frac{t_0 t_1 e^{i\delta_0}}{1 + r_0 r_1 e^{2i\delta_0}}, \quad (\text{S4})$$

where

$$\delta_0 = k_1 d = k_0 \tilde{n}_1 d, \quad (\text{S5})$$

and

$$M_{MR} = \frac{1}{1 + r_0 r_1 e^{2i\delta_0}} \quad (\text{S6})$$

is the multi-reflection factor.

With the distribution of strain induced by CAP, the amplitude transmission coefficient could be approximated by:

$$\begin{aligned} t' &= t_0 e^{i\delta} t_1 + t_0 e^{i\delta} r_1 r_p M_{MR} t_1 + t_0 \tilde{r}_p \tilde{r}_0 e^{i\delta} M_{MR} t_1 + \dots \\ &= \frac{t_0 t_1 e^{i\delta} (1 + r_1 M_{MR} r_p - r_0 M_{MR} \tilde{r}_p)}{1 + r_0 r_1 e^{2i\delta}}, \end{aligned} \quad (\text{S7})$$

where the first-order backscattering comes from the perturbative theory [S5-7]:

$$r_p = \frac{ik_0^2}{2k_1} \int_0^d \Delta\varepsilon(z, t) e^{2ik_1(d-z)} dz = ik_0 \frac{\partial \tilde{n}_1}{\partial \eta_{33}} \int_0^d \eta_{33}(z, t) e^{2ik_1(d-z)} dz, \quad (\text{S8})$$

$$\tilde{r}_p = \frac{ik_0^2}{2k_1} \int_0^d \Delta\varepsilon(z, t) e^{2ik_1 z} dz = ik_0 \frac{\partial \tilde{n}_1}{\partial \eta_{33}} \int_0^d \eta_{33}(z, t) e^{2ik_1 z} dz, \quad (\text{S9})$$

and the phase term:

$$\delta = \delta_0 + \Delta\delta, \quad (\text{S10})$$

$$\Delta\delta = \frac{k_0^2}{2k_1} \int_0^d \Delta\varepsilon(z, t) dz = k_0 \frac{\partial \tilde{n}_1}{\partial \eta_{33}} \int_0^d \eta_{33}(z, t) dz. \quad (\text{S11})$$

Omitting the second order term, we get

$$\frac{\delta t}{t} = \frac{t' - t}{t} \approx r_1 M_{MR} r_p - r_0 M_{MR} \tilde{r}_p + i\Delta\delta(1 - 2r_0 r_1 e^{2i\delta_0} M_{MR}). \quad (\text{S12})$$

We finally obtain

$$\begin{aligned} \frac{\Delta T}{T} = 2\text{Re} \left\{ ik_0 \frac{\partial \tilde{n}_1}{\partial \eta_{33}} \left[\frac{r_1}{1 + r_0 r_1 e^{2i\delta_0}} \int_0^d \eta_{33}(z, t) e^{2ik_1(d-z)} dz \right. \right. \\ \left. \left. - \frac{r_0}{1 + r_0 r_1 e^{2i\delta_0}} \int_0^d \eta_{33}(z, t) e^{2ik_1 z} dz + \left(\frac{1 - r_0 r_1 e^{2i\delta_0}}{1 + r_0 r_1 e^{2i\delta_0}} \right) \int_0^d \eta_{33}(z, t) dz \right] \right\}. \quad (\text{S13}) \end{aligned}$$

We also derive Eq. (S13) individually considering the Green function and transfer matrix.

S6. Global fitting

Here is the detail of the global fitting process. The left-hand side of Eq. (S13) is the experimentally measured $\Delta T/T$. The right-hand side contains the photoelastic coefficient and the strain-related integral, which we can calculate by our theoretical model. For samples of different thicknesses, the phase is different, hence leading to different constants preceding the integral. We therefore treat the photoelastic coefficient as the only global fitting parameter, while all phase- and thickness-dependent terms remain individually specific.

To perform the global fitting, we simultaneously fit the 20-, 25-, 30-, and 40-nm samples and search for the solution that minimizes the mean residual across all datasets. We use an initial guess of $\partial \tilde{n}/\partial \eta_{33} = 1 + i$, and add a small random perturbation and then run the procedure repeatedly to obtain the optimal photoelastic coefficient. The fitting is performed 1000 times, and the resulting distribution is used to extract the uncertainty, as shown by the error bars in Fig. 4(b). Finally, the photoelastic coefficient was evaluated as $\partial \tilde{n}/\partial \eta_{33} \sim 23.9(\pm 1.2) - i8.4(\pm 1.4)$ as discussed in the main text.

References

- [S1] T. Matsuda, T. Higo, T. Koretsune, N. Kanda, Y. Hirai, H. Peng, T. Matsuo, N. Yoshikawa, R. Shimano, S. Nakatsuji, and R. Matsunaga, Ultrafast Dynamics of Intrinsic Anomalous Hall Effect in the Topological Antiferromagnet Mn_3Sn , *Phys. Rev. Lett.* **130**, 126302 (2023).
- [S2] M. Ikhlas, T. Tomita, T. Koretsune, M.-T. Suzuki, D. Nishio-Hamane, R. Arita, Y. Otani, and S. Nakatsuji, Large anomalous Nernst effect at room temperature in a chiral antiferromagnet, *Nat. Phys.* **13**, 1085 (2017).
- [S3] K. Ono, Dynamic Viscosity and Transverse Ultrasonic Attenuation of Engineering Materials, *Appl. Sci.* **10**, 5265 (2020).
- [S4] U. Mehta, S. K. Yadav, I. Koirala, R. P. Koirala, G. K. Shrestha, and D. Adhikari, Study of surface tension and viscosity of Cu–Fe–Si ternary alloy using a thermodynamic approach, *Heliyon* **6**, e04674 (2020).
- [S5] C. Thomsen, H. T. Grahn, H. J. Maris, and J. Tauc, Surface generation and detection of phonons by picosecond light pulses, *Phys. Rev. B* **34**, 4129 (1986).
- [S6] O. Matsuda, M. C. Larciprete, R. Li Voti, and O.B. Wright, Fundamentals of picosecond laser ultrasonics, *Ultrasonics* **56**, 3 (2015).
- [S7] S. Wu, Z. Lu, A. Hu, X. Miao, F. Wang, Z. Sun, H. Yan, H. Zhang, and M. Ji, Dichroic Photoelasticity in Black Phosphorus Revealed by Ultrafast Coherent Phonon Dynamics, *J. Phys. Chem. Lett.* **12**, 5871 (2021).